

Strong and Tunable Electrical Anisotropy in Type-II Weyl Semimetal Candidate WP_2 with Broken Inversion Symmetry

Bo Su, Yanpeng Song, Yanhui Hou, Xu Chen, Jianzhou Zhao, Yongchang Ma, Yang Yang, Jiangang Guo, Jianlin Luo, and Zhi-Guo Chen*


A transition metal diphosphide, WP_2 , is a candidate for type-II Weyl semimetals (WSMs) in which spatial inversion symmetry is broken and Lorentz invariance is violated. As one of the prerequisites for the presence of the WSM state in WP_2 , spatial inversion symmetry breaking in this compound has rarely been investigated. Furthermore, the anisotropy of the WP_2 electrical properties and whether its electrical anisotropy can be tuned remain elusive. Angle-resolved polarized Raman spectroscopy, electrical transport, optical spectroscopy, and first-principle studies of WP_2 are reported. The energies of the observed Raman-active phonons and the angle dependences of the detected phonon intensities are consistent with results obtained by first-principle calculations and analysis of the proposed crystal symmetry without spatial inversion, showing that spatial inversion symmetry is broken in WP_2 . Moreover, the measured ratio (R_c/R_a) between the crystalline c -axis and a -axis electrical resistivities exhibits a weak dependence on temperature (T) in the temperature range from 100 to 250 K, but increases abruptly at $T \leq 100$ K, and then reaches the value of ≈ 8.0 at $T = 10$ K, which is by far the strongest in-plane electrical resistivity anisotropy among the reported type-II WSM candidates with comparable carrier concentrations. Optical spectroscopy study, together with the first-principle calculations on the electronic band structure, reveals that the abrupt enhancement of the electrical resistivity anisotropy at $T \leq 100$ K mainly arises from a sharp increase in the scattering rate anisotropy at low temperatures. More interestingly, the R_c/R_a of WP_2 at $T = 10$ K can be tuned from 8.0 to 10.6 as the magnetic field increases from 0 to 9 T. The so-far-strongest and magnetic-field-tunable electrical resistivity anisotropy found in WP_2 can serve as a degree of freedom for tuning the electrical properties of type-II WSMs, which paves the way for the development of novel electronic applications based on type-II WSMs.

A Weyl semimetal (WSM), which is a type of quantum matters with pairs of Weyl cones in the bulk and topologically protected Fermi arcs on the surface,^[1–10] offers an excellent platform for the realization of exotic phenomena, such as the chiral magnetic effect,^[11–17] high efficient catalysis,^[18,19] and quantum anomalous Hall effect.^[20] Two types of WSMs can be achieved by breaking spatial inversion symmetry or time reversal symmetry.^[1–10,20–27] Type-I WSMs can have closed point-like Fermi surfaces in the bulk, while type-II WSMs host open bulk Fermi surfaces and Weyl points at the boundary between electron and hole pockets.^[28–33] Furthermore, type-II WSMs are expected to possess unusual transport and optical properties which are distinct from those of type-I WSMs.^[34–37] However, to date, only a few type-II WSMs have been identified experimentally. A natural question to ask is whether a broader class of type-II WSMs with novel physical properties, such as strong and tunable electrical anisotropy, can be found experimentally.

Recently, a transition metal diphosphide, WP_2 , was theoretically predicted to be a candidate for type-II WSMs.^[32] Four pairs of Weyl points with opposite chirality are anticipated to be located below the Fermi level of WP_2 . Therein, the distance

B. Su, Y. Song, Y. Hou, X. Chen, Prof. Y. Yang, Prof. J. Guo, Prof. J. Luo, Prof. Z.-G. Chen
Beijing National Laboratory for Condensed Matter Physics
Institute of Physics
Chinese Academy of Sciences
Beijing 100190, China
E-mail: zgchen@iphy.ac.cn

B. Su, Y. Song, X. Chen, Prof. J. Guo, Prof. Z.-G. Chen
School of Physical Sciences
University of Chinese Academy of Sciences
Beijing 100190, China

 The ORCID identification number(s) for the author(s) of this article can be found under <https://doi.org/10.1002/adma.201903498>.

Y. Hou, Prof. Y. Ma
School of Materials Science and Engineering
Tianjin University of Technology
Tianjin 300384, China

Prof. J. Zhao
Co-Innovation Center for New Energetic Materials
Southwest University of Science and Technology
Mianyang, Sichuan 621010, China

Prof. Y. Yang, Prof. J. Guo, Prof. J. Luo, Prof. Z.-G. Chen
Songshan Lake Materials Laboratory
Dongguan, Guangdong 523808, China

Prof. J. Luo
Collaborative Innovation Center of Quantum Matter
Beijing, China

DOI: 10.1002/adma.201903498

between the two Weyl points of each pair in momentum space is so long that the nearest Weyl points have the same chirality. Since i) the positions of the Weyl points are sensitive to the small perturbations of the crystal structure, such as structural distortions and defects, and ii) the two Weyl points with opposite chirality would annihilate if they meet in momentum space, the same chirality of the neighboring Weyl points makes the predicted type-II WSM state of WP_2 particularly robust against structural distortions or defects. This distinguished character—the protection of the neighboring Weyl points with the same chirality against annihilation upon structural distortions or defects significantly reduces the probability of the scattering between the neighboring Weyl points and thereby plays an important role in the extremely low resistivity observed in WP_2 .^[38–40] In addition, the thermal and electrical transport measurements revealed that the WP_2 single crystals exhibit the transport behaviors of a hydrodynamic electron fluid: a viscosity-induced dependence of the electrical resistivity on the sample width and a strong violation of the Wiedemann–Franz law (i.e., the product of the thermal conductivity and the electrical resistivity, divided by the temperature is the Sommerfeld value which depends only on fundamental constants).^[41–43] However, to date, the anisotropy degree of the electrical resistivity within the crystalline ac -plane of WP_2 has not been explored by experiments. Furthermore, whether the anisotropy of the ac -plane resistivity of WP_2 can be tuned is still unclear. Generally, the electrical properties of solids are intimately associated with the crystal structures. Thus, investigating the crystal symmetry of WP_2 would be helpful in exploring and understanding the anisotropy degree of its electrical resistivity. Nevertheless, compared with the phosphorus positions of MoP_2 with non-centrosymmetric $Cmc2_1$ space group, the phosphorus positions of WP_2 , which are crucial for deriving its crystal symmetry, are less accurately determined by X-ray diffraction due to the larger discrepancy between the electron-density distributions of the transition-metal and phosphorus atoms. Moreover, for nonmagnetic WP_2 , the predicted Fermi arcs on the surface, which is a critical feature of a nonmagnetic Weyl semimetal with broken spatial inversion symmetry, has so far not been observed clearly by angle-resolved photoemission spectroscopy.^[38,44,45] Therefore, although WP_2 was proposed to be a promising type-II WSM candidate with remarkable properties, such as extremely low resistivity and hydrodynamic transport behaviors, one of the key prerequisites for the presence of the intriguing WSM state in WP_2 —spatial inversion symmetry breaking in this compound needs to be further confirmed.

Angle-resolved polarized Raman spectroscopy (ARPRS) is an experimental technique which is directly sensitive to the crystal symmetry. However, there are few ARPRS studies of WP_2 . Thus, a systematic investigation on the polarized Raman spectra of WP_2 is essential to fill the gap between the theoretical expectation of the spatial inversion symmetry breaking and the experimental confirmations. Here, we use ARPRS to check whether spatial inversion symmetry is broken in WP_2 . The measured Raman-active phonon energies and the angle dependences of the detected phonon intensities agree well with the results obtained by first-principle calculations and the analysis of the proposed $Cmc2_1$ space group without spatial inversion. The good consistence between the experimental

Raman data and theoretical results indicates spatial inversion symmetry breaking in WP_2 . The angle-dependent Raman-active phonon peak intensities not only indicate that the Raman-active phonon (or lattice) vibrations are anisotropic in WP_2 , but also manifest that ARPRS is a rapid and nondestructive tool to determine the crystallographic orientation of anisotropic type-II WSM candidates including WP_2 . Since the lattice structure of a material has a close relationship with its electrical properties, to investigate the degree of the electrical anisotropy, we carried out electrical resistivity measurements of the WP_2 single crystals at different temperatures and at different magnetic fields. Here, the ratio (i.e., R_c/R_a) between the electrical resistivity measured with the electric current (i.e., I) along the crystalline c -axis and the electrical resistivity measured with $I \parallel a$ -axis exhibits a weak dependence on temperature (T) (i.e., $R_c/R_a \approx 1.6$) in the temperature range from 100 to 250 K, but increases abruptly at $T \leq 100$ K, and then reaches the value of ≈ 8.0 at $T = 10$ K, which is by far the strongest electrical resistivity anisotropy among the reported type-II WSM candidates with their carrier concentrations comparable to $\approx 10^{21} \text{ cm}^{-3}$. Because optical spectroscopy is an efficient experimental tool for studying charge dynamics in materials, to study the origin of the abrupt increase in the resistivity anisotropy at low temperatures, we performed optical reflectance measurements on the WP_2 single crystals at different temperatures with the electrical field of the incident light applied along the crystalline c -axis and a -axis, respectively. Our optical spectroscopy study, together with the first-principle calculations on the electronic band structure, indicates that the steep enhancement of the electrical resistivity ratio R_c/R_a largely comes from a sharp increase in the scattering rate anisotropy at low temperatures. More interestingly, the R_c/R_a of WP_2 at $T = 10$ K can be tuned from 8.0 to 10.6 as the magnetic field (B) applied perpendicular to the crystalline ac -plane increases from 0 to 9 T. The strong and tunable anisotropy (1060% at $B = 9$ T and 800% at $B = 0$ T) of the in-plane (i.e., ac -plane) electrical resistivity can be considered as a degree of freedom for tuning the electrical properties of type-II WSMs.

WP_2 was proposed to crystallize in the space group of $Cmc2_1$ and has a non-centrosymmetric structure with a twofold screw axis along the crystalline c -axis, a glide plane perpendicular to the b -axis, and a mirror plane perpendicular to the a -axis,^[38] shown in Figure 1a. To study whether spatial inversion symmetry is broken in the crystal structure of WP_2 , we first used a 532 nm wavelength laser to measure the Raman spectra of the WP_2 single crystals at room temperature in the parallel-polarized configuration (i.e., the electrical field of the linearly polarized incident light E_i is parallel to the electrical field of the linearly polarized scattered light E_s , here $E_i \parallel E_s \parallel a$ -axis) and in the perpendicular-polarized configuration (i.e., $E_i \perp E_s$, here $E_i \parallel a$ -axis and $E_s \parallel c$ -axis), respectively (see the schematic of the configurations of the ARPRS in Figure 1b, the crystal orientation of the WP_2 single crystal characterized by single-crystal X-ray diffraction in the bottom-left inset of Figure 1b and the details about growing the single crystals, measuring the Raman spectra and determining the crystal orientation in the Experimental Section). Figure 1c displays the polarized Raman spectra of the WP_2 single crystals in the perpendicular- and parallel-polarized configurations. Three peak-like features can be observed in the perpendicular-polarized configuration, while

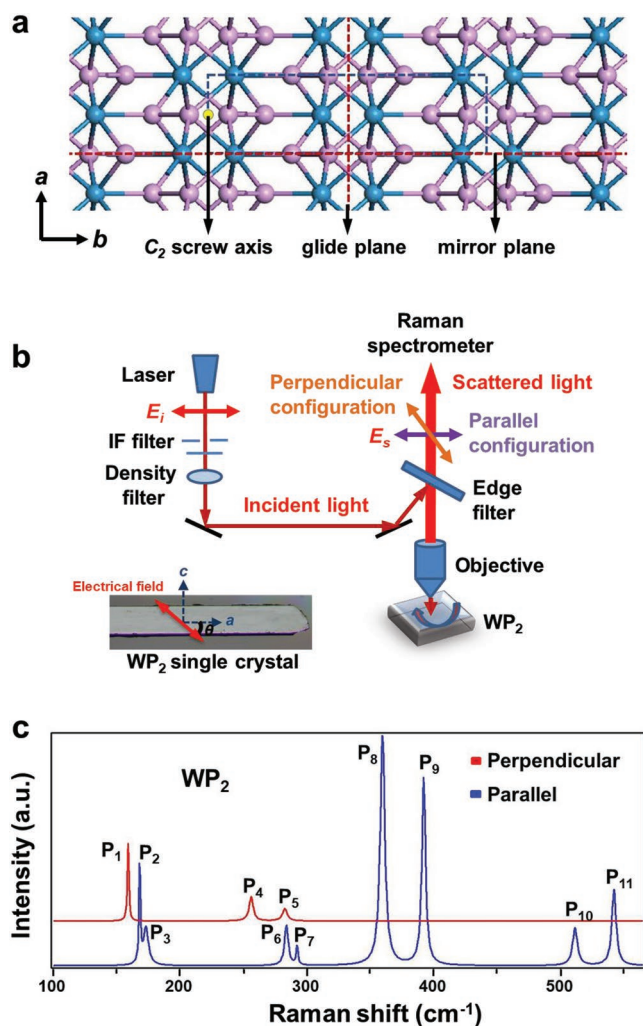


Figure 1. Crystal structure and polarized Raman spectra of WP₂. a) Crystal structure of WP₂. The W and P atoms are denoted by the light cyan and pink spheres, respectively. The cyan dashed box shows the orthorhombic conventional unit cell. The C₂ screw axis along the crystalline *c*-axis is shown by the yellow dot. The glide and mirror planes are indicated by the two red dashed lines, respectively. b) Schematic of the angle-resolved polarized Raman spectroscopy (ARPRS). The electrical fields of the linearly polarized incident and scattered lights are *E_i* and *E_s*, respectively. The bottom-left inset depicts the optical image of the WP₂ single crystal measured by ARPRS. c) Raman spectra of the WP₂ single crystal which were measured in the parallel-polarized (i.e., *E_i* // *E_s* // *a*-axis) and perpendicular-polarized (i.e., *E_i* ⊥ *E_s*, *E_i* // *a*-axis, and *E_s* // *c*-axis) configurations, respectively. Several peak-like features are present in the polarized Raman spectra of WP₂.

eight peak-like features are present in the parallel-polarized configuration. To study the nature of the probed peak-like features, we performed the analysis of the proposed *Cmc*2₁ space group. Since i) the proposed *Cmc*2₁ space group belongs to the C_{2v} point group, and ii) the 6 atoms of its unit cell correspond to 18 phonon modes, the phonon modes of WP₂ should be decomposed into 18 irreducible representations: [5A₁ + 3A₂ + 2B₁ + 5B₂] + [5A₁ + 2B₁ + 5B₂] + [A₁ + B₁ + B₂], where the first, second, and third terms represent the Raman-active, infrared-active, and the acoustic phonon modes, respectively (see the

elaboration on the derivation of the irreducible representations in Section S1 of the Supporting Information). Therein, the symmetry of the Raman-active phonons is determined by the corresponding Raman tensors (*R*) of the C_{2v} point group

$$\mathbf{R}(A_1) = \begin{pmatrix} a & 0 & 0 \\ 0 & b & 0 \\ 0 & 0 & c \end{pmatrix}, \mathbf{R}(A_2) = \begin{pmatrix} 0 & d & 0 \\ d & 0 & 0 \\ 0 & 0 & 0 \end{pmatrix} \quad (1)$$

$$\mathbf{R}(B_1) = \begin{pmatrix} 0 & 0 & e \\ 0 & 0 & 0 \\ e & 0 & 0 \end{pmatrix}, \mathbf{R}(B_2) = \begin{pmatrix} 0 & 0 & 0 \\ 0 & 0 & f \\ 0 & f & 0 \end{pmatrix} \quad (2)$$

where the *a*, *b*, *c*, *d*, *e*, and *f* are the tensor elements and their values depend on the cross-section of Raman scattering. Moreover, the intensity (*I_{ph}*) of the Raman-active phonon has the following relationship with the polarization states of the incident light *e_i* and the scattered light *e_s* and *R*^[46]

$$I_{ph} \propto |\mathbf{e}_i \cdot \mathbf{R} \cdot \mathbf{e}_s|^2 \quad (3)$$

On the basis of the irreducible representations of the C_{2v} point group, the above Raman tensors and the above relationship among the phonon intensity, the Raman tensors, and the polarization states of the incident and scattered lights, we can obtain that i) five A₁ Raman-active phonon modes and three A₂ Raman-active phonon modes can be observed under the parallel-polarized (i.e., *E_i* // *E_s* // *a*-axis) and perpendicular-polarized (i.e., *E_i* ⊥ *E_s* and *E_s* // *c*-axis) configurations, respectively, and that ii) two B₁ and five B₂ Raman-active phonon modes can be detected only when the polarized electrical field *E_i* or *E_s* is aligned along the *b*-axis which is perpendicular to the *ac*-plane. Using first-principle calculations, we got the theoretical energies of the Raman-active phonon modes in WP₂ (see the details about our first-principle calculations in the Experimental Section). The energies of the calculated phonon modes and the measured peak-like features are listed in Table 1 (see the calculated phonon band dispersions of WP₂ along the high-symmetry lines in Figure S2b of the Supporting Information). According to the above group analysis and the consistence between the theoretical and experimental Raman-active phonon energies, i) the three measured peak-like features, P₁ at 159.2 cm⁻¹, P₄ at 256.3 cm⁻¹, and P₅ at 282.2 cm⁻¹, which are measured in the perpendicular-polarized configuration, can be assigned to the three Raman-active phonon modes 3A₂, and ii) the five measured peak-like features, P₂ at 168.4 cm⁻¹, P₆ at 284.1 cm⁻¹, P₈ at 359.9 cm⁻¹, P₉ at 392.4 cm⁻¹, and P₁₀ at 511.7 cm⁻¹, which are measured in the parallel-polarized configuration, can be ascribed to the five Raman-active modes 5A₁ (see the discussion about the three peak-like features, P₃, P₇, and P₁₁ in Section S2 of the Supporting Information). Figure 2 shows the atomic schematics of the calculated phonon vibrational patterns for the five Raman-active phonon modes 5A₁ in the parallel-polarized configuration and the three Raman-active phonon modes 3A₂ in the perpendicular-polarized configurations (see the vibrational patterns for the seven Raman modes, 2B₁ + 5B₂, in Figure S3 of the Supporting Information). Besides the non-centrosymmetric structure with the space group *Cmc*2₁ discussed above, WP₂ can crystallize in a centrosymmetric

Table 1. The calculated Raman-active and infrared-active (IR) phonon modes, and experimental Raman-active phonon modes of WP₂ with their irreducible representations at room temperature.

Symmetry	Activity	Calculated energy [cm ⁻¹]	Experiment energy [cm ⁻¹]
A ₂	Raman	157.4	159.2 (P ₁)
B ₂	Raman + IR	166.8	
A ₁	Raman + IR	168.4	168.4 (P ₂)
B ₁	Raman + IR	250.3	
A ₂	Raman	250.7	256.3 (P ₄)
A ₂	Raman	275.8	282.2 (P ₅)
A ₁	Raman + IR	277.4	284.1 (P ₆)
B ₂	Raman + IR	284.3	
B ₁	Raman + IR	311.7	
A ₁	Raman + IR	341.8	359.9 (P ₈)
B ₂	Raman + IR	346.8	
A ₁	Raman + IR	381.0	392.4 (P ₉)
B ₂	Raman + IR	432.1	
A ₁	Raman + IR	498.2	511.7 (P ₁₀)
B ₂	Raman + IR	525.7	

structure with the space group C12/m1, which has spatial inversion symmetry and belongs to the C_{2h} point group.^[47,48] After performing the analysis of the possible centrosymmetric space group C12/m1, we found that the phonon modes of WP₂ corresponding to this space group should be decomposed into 18 irreducible representations: [6A_g + 3B_g] + [2A_u + 4B_u] + [A_u + 2B_u], where the first, second, and third terms represent

the Raman-active, infrared-active, and the acoustic phonon modes, respectively. In the centrosymmetric space group of WP₂, the parity-even A_g (or B_g) and the parity-odd A_u (or B_u) representations are exclusive with each other. The Raman tensors (R) of the C_{2h} point group, which correspond to the A_g and B_g Raman-active phonon modes, can be written as

$$\mathbf{R}(A_g) = \begin{pmatrix} a & d & 0 \\ d & b & 0 \\ 0 & 0 & c \end{pmatrix}, \mathbf{R}(B_g) = \begin{pmatrix} 0 & 0 & e \\ 0 & 0 & f \\ e & f & 0 \end{pmatrix} \quad (4)$$

According to the irreducible representations of the C_{2h} point group, the corresponding Raman tensors and the relationship among the phonon intensity, the Raman tensors, and the polarization states of the incident and scattered lights (i.e., Equation (3)), only six A_g Raman-active phonon modes can be observed in the perpendicular-polarized or parallel-polarized configuration. Thus, the only two space

groups (i.e., Cmc2₁ with broken inversion symmetry and C12/m1 with inversion symmetry) of WP₂ have different numbers of Raman-active phonon modes in the perpendicular-polarized and parallel-polarized configurations (the consistency between the numbers of the measured Raman-active phonon modes in Figure S2a of the Supporting Information measured by the 532 nm wavelength laser and the 633 nm wavelength laser in the parallel-polarized configuration suggests that the assignment of the group symmetry of WP₂ is unlikely to be influenced by the wavelength of the laser used for the Raman measurements^[49]). Moreover, our polarized Raman measurements of WP₂ show three peak-like features in the perpendicular-polarized configuration and eight peak-like features in the parallel-polarized configuration. Therefore, the inconsistency between the numbers of the measured peak-like features in Figure 1c and the theoretical Raman-active phonon modes obtained based on the centrosymmetric space group C12/m1 with inversion symmetry indicates that the crystal structure of the WP₂ single crystals here is unlikely to belong to the centrosymmetric space group C12/m1 with inversion symmetry.

To further investigate whether spatial inversion symmetry is broken in WP₂, we performed the crystal-angle-resolved Raman measurements at room temperature under the parallel-polarized (i.e., E_i // E_s) and perpendicular-polarized (i.e., E_i ⊥ E_s) configurations with E_i and E_s parallel to the crystalline *ac*-plane using a 532 nm wavelength laser. The polarized Raman spectra were measured by rotating the WP₂ single crystal within its *ac*-plane and altering the angle θ between the rotated crystal-line *a*-axis and the fixed electrical field of the linearly polarized incident light E_i (see the schematic of the experimental setup for the crystal-angle-resolved polarized Raman measurements in Figure 1b). Figure 3a,b depicts the crystal-angle-dependent Raman spectra of the WP₂ single crystals measured in the parallel-polarized configuration and the corresponding contour

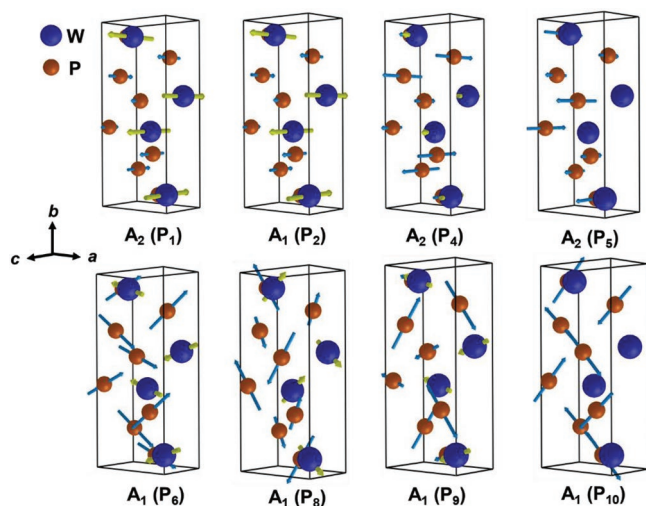


Figure 2. Atomic schematics of the calculated vibrational patterns of the Raman-active phonon modes A₁ and A₂. The Raman-active modes A₁ and A₂ of WP₂ can be observed under the parallel-polarized (i.e., E_i // E_s // *a*-axis) and perpendicular-polarized (i.e., E_i ⊥ E_s, E_i // *a*-axis and E_s // *c*-axis) configurations, respectively. The three measured peak-like features, P₁, P₄, and P₅, can be assigned to the three Raman-active phonon modes 3A₂. The five measured peak-like features, P₂, P₆, P₈, P₉, and P₁₀ can be ascribed to the five Raman-active modes 5A₁. The W and P atoms in the unit cell are denoted by blue and brown spheres, respectively. The atomic displacements of the W and P atoms are indicated by the colored arrows.

map of the angle-dependent Raman intensity, respectively (see the angle-dependent Raman spectra in the perpendicular configuration in Figure S4 and the related discussion in Section S3 of the Supporting Information). The peak-like features, P_1 , P_2 , P_4 , P_6 , P_8 , P_9 , and P_{10} , which correspond to the Raman-active phonon modes A_1 and A_2 , respectively, can be observed in the angle-dependent Raman spectra under both the parallel-polarized and perpendicular-polarized configurations because when the WP_2 single crystal is rotated within its ac -plane, the electrical fields of the linearly polarized incident and scattered lights, E_i and E_s , can have the two components which are along the a -axis and c -axis, respectively. As shown in Figure 3c–i, under the parallel-polarized configuration, the angle dependences of the intensities of the A_1 phonon peaks, P_2 , P_6 , P_8 , P_9 , and P_{10} , exhibit a two-lobed shape with two maximum intensities. For the A_1 phonon peaks, P_6 and P_{10} have two maximum intensities at angles $\theta = 90^\circ$ and 270° , while P_2 , P_8 , and P_9 show two maximum intensities at angles $\theta = 0^\circ$ and 180° . By contrast, under the parallel-polarized configuration, the angle dependences of the intensities of the A_2 phonon peaks, P_1 and P_4 , display a four-lobed shape with four maximum intensities at angles $\theta = 45^\circ$, 135° , 225° , and 315° . To quantitatively check whether the variation of the A_1 and A_2 phonon peak intensities are consistent with the spatial inversion symmetry breaking in the WP_2 crystal structure, we need to calculate the angle dependences of the A_1 and A_2 phonon peak intensities based on Equation (3). Under the parallel-polarized configuration, the polarization states of the incident e_i and the scattered light e_s can be expressed as $e_i = e_s = (\cos\theta, \sin\theta, 0)$. According to Equation (3), the intensities of the A_1 and A_2 phonon peaks are given by^[50–53]

$$I_{A_1}'' \propto a^2 \cos^4 \theta + b^2 \sin^4 \theta + 2ab \cos^2 \theta \sin^2 \theta \cos \phi_{ab} \quad (5)$$

$$I_{A_2}'' \propto d^2 \sin^2 2\theta \quad (6)$$

where ϕ_{ab} is the phase difference between the Raman tensor elements a and b . Equations (5) and (6) indicate that in the parallel-polarized configurations, the A_1 phonon peak intensities vary with a period of 180° , while the variation of the A_2 phonon peak intensities has a period of 90° with the maximum intensities at angles $\theta = 45^\circ$, 135° , 225° , and 315° , and the minimum intensities at angles $\theta = 0^\circ$, 90° , 180° , and 270° . Figure 3c–i shows that the angle dependences of the A_1 and A_2 phonon peak intensities measured in the parallel-polarized configuration can be consistently fitted by Equations (5) and (6). Moreover, the angles of the maximal intensities of these Raman-active phonon peaks measured using ARPRS are not consistent with those corresponding to the centrosymmetric space group $C12/m1$, which further indicates that the crystal structure of the WP_2 single crystals here should not belong to the centrosymmetric space group $C12/m1$ with inversion symmetry (see the detailed discussion in Section S4 of the Supporting Information). The good agreement between the angle dependences of the Raman-active phonon peak intensities measured using ARPRS (see the red dots in Figure 3c–i) and the fitting results based on the broken spatial inversion symmetry of the WP_2 crystal structure (see the red curves in Figure 3c–i), combined with the consistence between

the energies of the peaks observed in the polarized Raman spectra and the calculated Raman-active phonon energies, provides convincing evidence for the spatial inversion symmetry breaking in the type-II Weyl semimetal candidate WP_2 by a combination of linearly polarized Raman measurements and first-principle calculations.

It is worth noticing that since the naturally grown WP_2 single crystals sometimes have arbitrary shapes (see Figure S6 in the Supporting Information), the crystallographic orientation of the naturally grown crystals cannot be always determined. In the parallel-polarized configuration, the variation of the A_1 phonon peak intensities has a variation period of 180° and the maximum intensities appear when the electrical field of the linearly polarized incident light E_i is applied along the crystalline a -axis or c -axis, while the A_2 phonon peak intensities vary with a period of 90° . Therefore, the A_1 phonon peaks can be used to determine the crystallographic orientation of the WP_2 single crystal. Whether the maxima of the A_1 phonon peak intensity correspond to the crystalline a -axis or c -axis lies with the relative magnitude of the Raman tensor elements a and b for the A_1 phonon peak. According to Equation (5), when the Raman tensor elements $a > b$, the maximum intensities of the A_1 phonon peaks point to the a -axis; when the Raman tensor elements $a < b$, the maximum intensities of the A_1 phonon peaks are along the c -axis. Therefore, the crystallographic orientation of the WP_2 single crystals can be identified by the maximum intensities of the A_1 phonon peaks as long as the relative magnitude of Raman tensor elements a and b has been confirmed. We experimentally obtained that in WP_2 , the Raman tensor elements $a > b$ for the P_2 , P_8 , and P_9 peak-like features and that the Raman tensor elements $a < b$ for the P_6 and P_{10} peak-like features using polarized Raman spectroscopy and single-crystal X-ray diffraction on the same single crystal. Thus, the crystal-angle-resolved polarized Raman spectroscopy provides a rapid and nondestructive method for determining the crystal orientation of the WP_2 single crystal and other type-II WSMs.^[50,51,54–58]

As revealed by ARPRS, the angle-dependent Raman-active phonon peak intensities further indicate the anisotropy of the Raman-active phonon (or lattice) vibrations in WP_2 . Usually, the lattice structures of solids are closely related to the electrical properties. Thus, the electrical properties of WP_2 are expected to be anisotropic. Nevertheless, the anisotropy degree of the electrical properties of WP_2 remains unclear. To study the anisotropy degree of the electrical properties of WP_2 , we measured the electrical resistivities of its single crystals at different temperatures with the electric currents (i.e., I) applied along the two crystalline directions— c -axis and a -axis, respectively (see the details about the electrical resistivity measurements in the Experimental Section). Figure 4a shows the temperature (i.e., T) dependences of the c -axis and a -axis resistivities (i.e., R_c and R_a) on a logarithmic scale (see the R_c and R_a on the original scale in the inset of Figure 4a). The discrepancy between the R_c and the R_a can be observed clearly in Figure 4a and its inset. To investigate the anisotropy of the in-plane (i.e., ac -plane) electrical resistivity of the WP_2 single crystals, we plotted the ratio between the R_c and the R_a (i.e., R_c/R_a) as a function of temperature in Figure 4b. In the temperature range from 100 to 250 K, the R_c/R_a shows a weak dependence on temperature and have the value of ≈ 1.6 . Surprisingly, at $T \leq 100$ K,

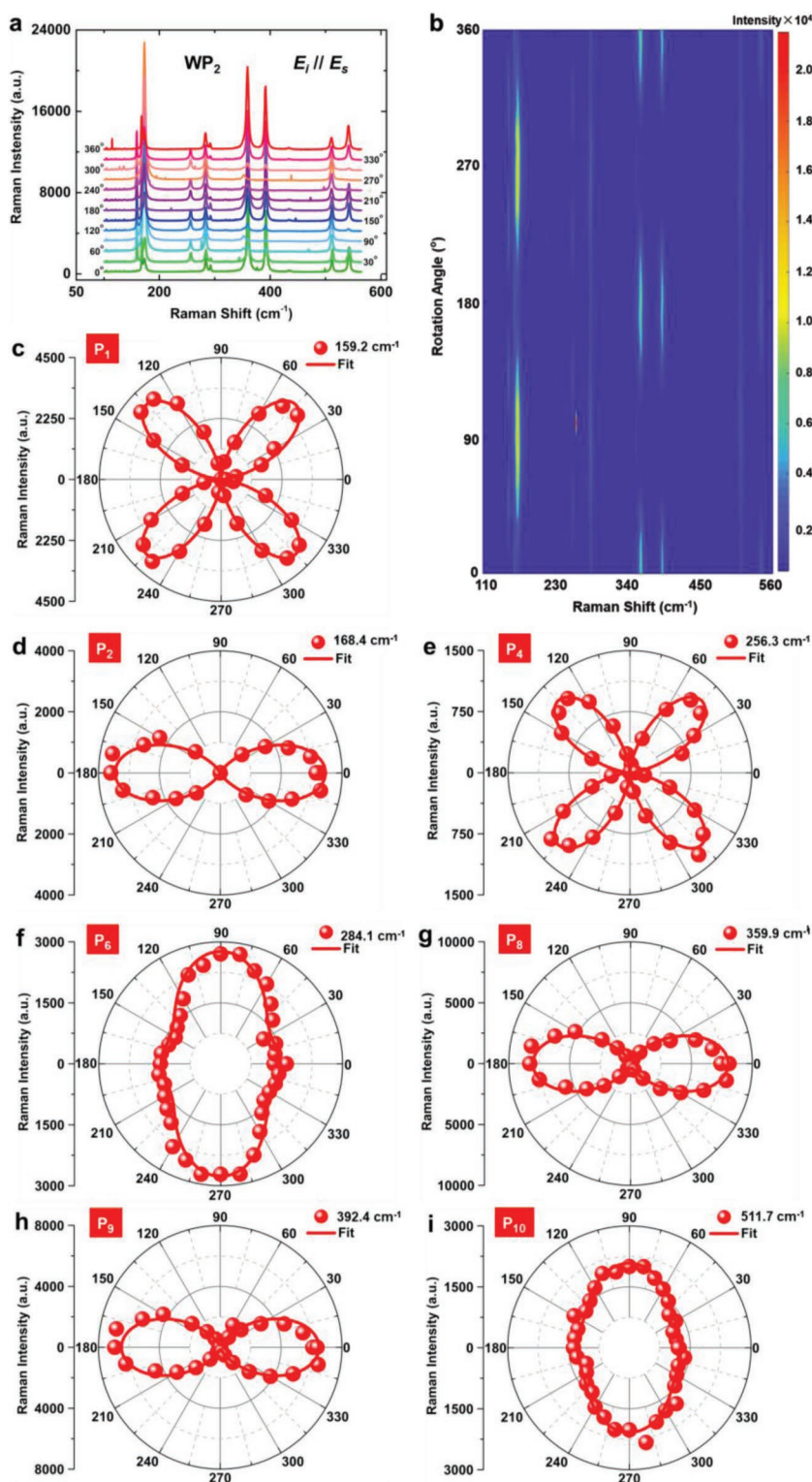


Figure 3. Angle dependences of the intensities of the A₁ and A₂ phonon peaks measured in the parallel-polarized configuration. a) Angle-dependent Raman spectra of the measured WP₂ single crystals. b) Contour map of the measured Raman phonon intensities as a function of angle and energy. c–i) Angle dependences of the Raman-active phonon peak intensities. The red dots show the measured data. The red solid curves display the fitting results based on Equations (5) and (6).

the resistivity ratio R_c/R_a of WP₂ increases sharply and then reaches the value of ≈ 8.0 at 10 K (the relative resistivity ratio $\Delta R_c/R_a$ in the inset of Figure 4b, which was obtained by subtracting a linear T dependence of the R_c/R_a shown in the temperature range from 150 to 200 K from the R_c/R_a , clearly shows a sharp increase at $T \leq 100$ K), which is by far the strongest in-plane electrical resistivity anisotropy among the reported type-II WSM candidates (such as MoTe₂ and TaIrTe₄) with their carrier densities comparable to $\approx 10^{21} \text{ cm}^{-3}$.^[38,50,59,60]

In order to investigate the origin of the abrupt increase in the electrical resistivity anisotropy of WP₂, we calculated its electronic band structure and performed optical reflectance measurements on its single crystals with the electric field (E) of the incident light applied along its crystalline c -axis and a -axis, respectively (see the details about the theoretical calculations and optical reflectance measurements in the Experimental Section). Figure 4c shows the electronic band structure of WP₂ obtained by first-principle calculations. The upper left and right insets of Figure 4c display the positions of the four pairs of Weyl points in the Brillouin zone and the Fermi surfaces, respectively. According to the positions of the Weyl points (e.g., W₁) in the Brillouin zone, the band dispersions near the Weyl points (e.g., the band dispersion near W₁ in Figure 4c) contribute to the butterfly like Fermi surfaces in the upper right inset of Figure 4c.^[32,38] Since the electrical transport properties of a material are intimately associated with the electronic states near the Fermi energy (E_F), to study the in-plane electrical resistivity anisotropy in WP₂, we focus on the electronic bands which disperse parallel to the k_x - and k_z -axes, respectively, and cross the Fermi level. The calculated band dispersion along the k_x -axis (i.e., the high-symmetry line Γ –X of the Brillouin zone) has an effective mass m_x^* of $\approx 1.8 m_0$ at E_F . Moreover, at E_F , the effective masses m_z^* of the electronic bands dispersing parallel to the k_z -axis (i.e., the high-symmetry lines S–R and X₁–A₁) are about $1.4 m_0$ and $1.1 m_0$, respectively. Therefore, the ratio (i.e., m_z^*/m_x^*) between the effective masses of the electronic bands dispersing parallel to the k_z - and k_x -axes is smaller than unity. Considering that i) the resistivity in a conventional metallic state can be given by $R = m^*/(e^2 n \tau)$ (here e is the elementary charge, n is the carrier concentration, and τ^{-1} is the scattering rate),^[41]

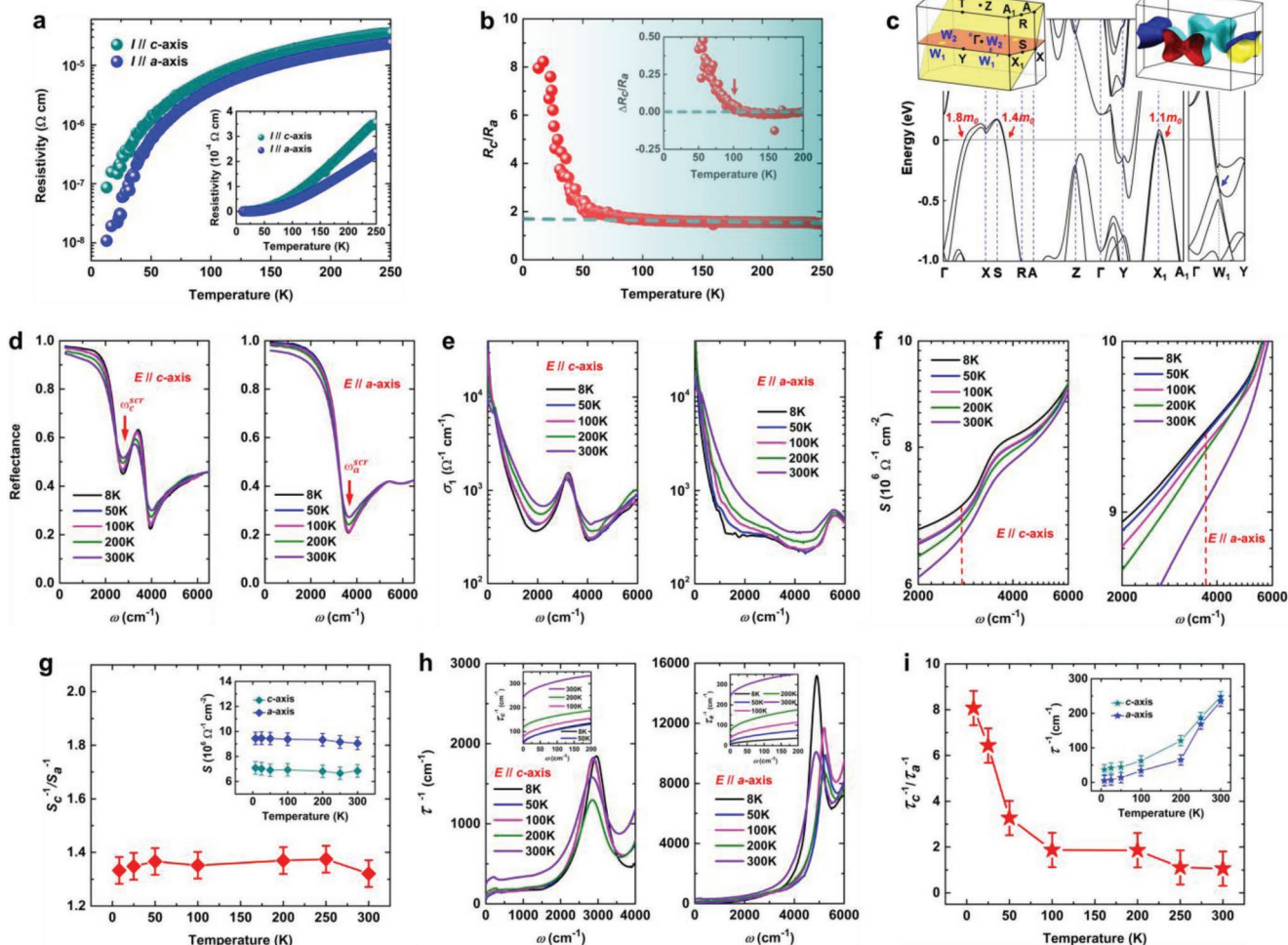


Figure 4. In-plane resistivity anisotropy and optical study of charge dynamics in the WP_2 single crystals. a) Temperature dependence of the resistivities on a logarithmic scale. The resistivities were measured with the electric currents (i.e., I) applied along the c -axis and a -axis, respectively. The resistivities were plotted on the original scale in the bottom-right inset. b) Ratio between the c -axis and a -axis resistivities as a function of temperature (T). The inset displays the relative resistivity ratio $\Delta R_c/R_a$ obtained by subtracting the linear T dependence of the resistivity ratio (see the dashed line in (b)). The red arrow indicates the onset temperature of an abrupt increase in the $\Delta R_c/R_a$. c) Calculated band dispersions along the high-symmetry lines of the Brillouin zone and near the Weyl point W_1 . The upper left and right insets show four pairs of Weyl points in the Brillouin zone and the Fermi surfaces, respectively. d) Reflectance spectra measured with the electric field $E \parallel c$ -axis (the left panel) and $E \parallel a$ -axis (the right panel). The two red arrows in the left and right panels indicate the screened plasma frequencies ω_{sc}^c and ω_{sc}^a which correspond to the incident light with $E \parallel c$ -axis and $E \parallel a$ -axis, respectively. e) Real parts σ_1 of the optical conductivity with $E \parallel c$ -axis (the left panel) and $E \parallel a$ -axis (the right panel). f) Spectral weights (S) of the σ_1 with $E \parallel c$ -axis and $E \parallel a$ -axis. The two dashed vertical lines in the left and right panels are guides for eye showing the screened plasma frequencies. g) Ratio S_c^{-1}/S_a^{-1} between the reciprocals of the Drude weights with $E \parallel c$ -axis and $E \parallel a$ -axis at different temperatures. The Drude weights S_c and S_a were plotted in the inset as a function of T . h) Scattering rate spectra $\tau_c^{-1}(\omega)$ and $\tau_a^{-1}(\omega)$ obtained with $E \parallel c$ -axis (the left panel) and $E \parallel a$ -axis (the right panel). The insets display the magnified views of the $\tau_c^{-1}(\omega)$ and $\tau_a^{-1}(\omega)$. i) Ratio τ_c^{-1}/τ_a^{-1} at different temperatures. The inset shows the T dependences of the τ_c^{-1} and τ_a^{-1} .

and ii) the effective mass ratio m_z^*/m_x^* is much less than the resistivity ratio R_c/R_a at 10 K, the sudden increase in the electrical resistivity anisotropy of WP_2 at $T \leq 100$ K is unlikely to arise from the anisotropic effective mass of its electronic structure.

Optical spectroscopy is an efficient experimental technique for investigating charge dynamics in solids.^[61–67] In order to further study the roles of the anisotropies of the carrier concentration n , effective mass m^* , and scattering rate τ^{-1} in the emergence of the sharp increase in the electrical resistivity anisotropy, we carried out optical reflectance measurements on the WP_2 single crystals with $E \parallel c$ -axis and $E \parallel a$ -axis at different

temperatures. Figure 4d displays several representative reflectance spectra $R(\omega)$. Sharp plasma edges are present in the low-energy regions of the c -axis and a -axis $R(\omega)$. The screened plasma frequencies of the c -axis and a -axis $R(\omega)$, which correspond to the energy positions of the minima of the plasma edges, $\omega_{\text{sc}}^c \approx 2750 \text{ cm}^{-1}$ and $\omega_{\text{sc}}^a \approx 3651 \text{ cm}^{-1}$ (see the two red arrows in Figure 4d). Given that i) the square of the plasma frequency, which has the form $\omega_p^2 = 4\pi n e^2 / m^*$, is proportional to n/m^* , and ii) the ω_p^2 scales linearly with the spectral weight (i.e., Drude weight S) of the Drude component of the real part of the optical conductivity $\sigma_1(\omega)$, which can be estimated

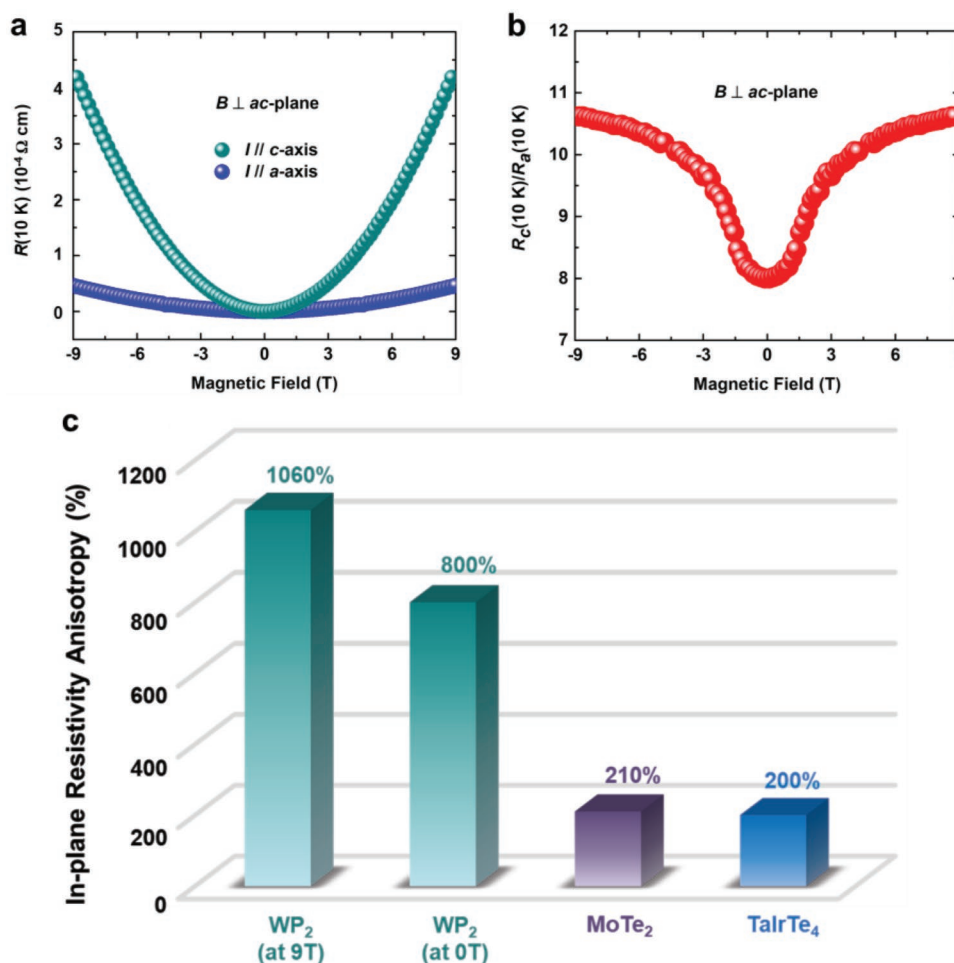


Figure 5. In-plane resistivity anisotropies of a type-II Weyl semimetal candidate WP_2 at magnetic fields. a) Magnetic-field-dependent resistivities measured at temperature $T = 10\text{ K}$ with the magnetic field (i.e., B) perpendicular to the ac -plane and the electric currents along the a -axis and c -axis. b) Ratio between the c -axis and a -axis resistivities at 10 K as a function of magnetic field. The ratio between the c -axis and a -axis resistivities at $T = 10\text{ K}$ goes up to ≈ 10.6 at $B = 9\text{ T}$. c) Reported in-plane resistivity anisotropies of the promising type-II Weyl semimetal candidates with their carrier densities comparable to 10^{21} cm^{-3} .

by integrating the $\sigma_1(\omega)$ up to the screened plasma frequency, i.e., $\omega_p^2 = 8S \approx 8 \int_0^{\omega_{sc}} \sigma_1(\omega) d\omega$, we need to get the $\sigma_1(\omega)$ of the WP_2 single crystals by the Kramers–Kronig transformations of the measured $R(\omega)$ and then to obtain the spectral weight $S(\omega)$ of the $\sigma_1(\omega)$.^[59–65] Figure 4e,f shows the $\sigma_1(\omega)$ and the $S(\omega)$, respectively (see the details about the Kramers–Kronig transformation in the Experimental Section). Therein, the Drude weight S corresponds to the $S(\omega)$ at the screened plasma frequency (see the red dashed lines in Figure 4f). As shown in Figure 4g, the ratio (i.e., S_c^{-1}/S_a^{-1}) between the reciprocals of the c -axis and a -axis Drude weights (i.e., S_c^{-1} and S_a^{-1}) is about 1.3 and exhibits a quite weak dependence on T . Because i) $(\omega_p^2)^{-1} \propto m^*/n \propto S^{-1}$, ii) the weak T -dependence of the S_c^{-1}/S_a^{-1} is in sharp contrast to the abrupt increase in the R_c/R_a at low temperatures, iii) the S_c^{-1}/S_a^{-1} is much smaller than the R_c/R_a of ≈ 8 at 10 K , the sudden increase in the electrical resistivity anisotropy of WP_2 should not be mainly caused by the anisotropy of the m^*/n (or the S^{-1}). Furthermore, we derived the scattering rate spectra $\tau^{-1}(\omega)$ by performing the extended Drude

analysis of the optical data (see Figure 4h and the details about the extended Drude analysis in the Experimental Section).^[61–63] We plotted the c -axis and a -axis scattering rate at $\omega = 0$ (i.e., τ_c^{-1} and τ_a^{-1}) as a function of temperature in the inset of Figure 4i. As shown in Figure 4i, the ratio τ_c^{-1}/τ_a^{-1} between the τ_c^{-1} and τ_a^{-1} increases rapidly at $T \leq 100\text{ K}$ and reaches the value of ≈ 8.0 at 10 K , which is consistent with the T -dependence of the R_c/R_a . Therefore, the consistency between the T -dependences of the ratios τ_c^{-1}/τ_a^{-1} and R_c/R_a indicates that the rapid enhancement of the scattering rate anisotropy at $T \leq 100\text{ K}$ is the main factor giving rise to the abrupt increase in the electrical resistivity anisotropy at low temperatures.

It is worth noticing that in contrast to the pairs of neighboring Weyl points with opposite chirality in the previously reported type-II WSM candidates, such as $MoTe_2$ and $TaIrTe_4$, the neighboring Weyl points in WP_2 have the same chirality.^[32,38] For WP_2 , this distinguished character—the protection of the neighboring Weyl points with the same chirality against annihilation upon structural distortions or defects can significantly reduce the probability of the scattering between its

neighboring Weyl points.^[38] Moreover, these neighboring Weyl points in WP_2 are located within the same k_x – k_y -plane, which implies that the scattering rate within the k_x – k_y -plane may be much smaller than the scattering rates within the other planes including the k_z -direction. Therefore, one possible physical source of the scattering rate anisotropy (i.e., τ_c^{-1}/τ_a^{-1}) may be related to the significantly reduced probability of the scattering between its neighboring Weyl points with the same chirality in the same k_x – k_y -plane. In this regard, since the pairs of neighboring Weyl points in the reported type-II WSM candidates have opposite chirality, the neighboring Weyl points with the same chirality in the same k_x – k_y -plane may make the scattering rate anisotropy in WP_2 different from those in the reported type-II WSM candidates, such as $MoTe_2$ and $TaIrTe_4$. In addition, previous theoretical studies suggest that for a WSM at low temperatures, its disorders, and the anisotropy of the Fermi velocity of Weyl fermions can induce the resistivity anisotropy, e.g., $R_c/R_a \sim (v_a/v_c)^2$, where v_a and v_c are the Fermi velocities of Weyl fermions along the a -axis and c -axis, respectively.^[68] In WP_2 , $v_a/v_c \approx 10$,^[32] so $R_c/R_a \approx 100$, which is much larger than the measured resistivity anisotropy at $T = 10$ K. Perhaps, its resistivity anisotropy induced by the disorders and the Fermi velocity anisotropy may be weakened by its topologically trivial bands and then reach the anisotropy degree of its resistivity at $T = 10$ K.

To further study whether the electrical resistivity ratio R_c/R_a of the WP_2 single crystals can be tuned, we performed the electrical resistivity measurements at $T = 10$ K with the magnetic field applied perpendicular to the crystalline ac -plane. Figure 5a displays the magnetic-field-dependent resistivities measured with the electric currents along the c -axis and a -axis, respectively. It can be observed that the difference between the R_c and the R_a grows continuously with increasing magnetic fields. Then, we plotted the electrical resistivity ratio $R_c(10\text{ K})/R_a(10\text{ K})$ at $T = 10$ K as a function of magnetic field (B) in Figure 5b. The electrical resistivity ratio $R_c(10\text{ K})/R_a(10\text{ K})$ increases from ≈ 8.0 to ≈ 10.6 as the magnetic field is enhanced from 0 to 9 T, which manifests that the magnetic field can effectively tune the resistivity ratio $R_c(10\text{ K})/R_a(10\text{ K})$ (see Figure 5c). The strong and tunable anisotropy of the in-plane (i.e., ac -plane) electrical resistivity found in WP_2 can act as a degree of freedom for tuning the electrical properties of type-II WSMs and thus have potential applications in new generation of electronic devices.^[69–71]

In summary, we have performed the electrical transport, optical spectroscopy, first-principle, and ARPES studies of the type-II WSM candidate in WP_2 . The ratio (R_c/R_a) between the crystalline c -axis and a -axis electrical resistivities shows a weak dependence on temperature in the temperature range from 100 to 250 K, but increases suddenly at $T \leq 100$ K, and then reaches the value of ≈ 8.0 at $T = 10$ K, which is by far the strongest in-plane electrical resistivity anisotropy among the known type-II WSM candidates with their carrier concentrations comparable to $\approx 10^{21}\text{ cm}^{-3}$. Our optical spectroscopy study, combined with the first-principle calculations on the electronic band structure, indicates that the sudden increase in the electrical resistivity anisotropy at $T \leq 100$ K mainly originates from the sharp enhancement of the scattering rate anisotropy at low temperatures. Moreover, the R_c/R_a of WP_2 at $T = 10$ K can be tuned from 8.0 to 10.6 as the magnetic field was enhanced from

0 to 9 T. The strong and tunable electrical resistivity anisotropy found in WP_2 can be considered as a degree of freedom for tuning the electrical properties of type-II WSMs. In addition, the good agreement between the angle dependences of the Raman-active phonon peak intensities measured using ARPES and the fitting results based on the broken spatial inversion symmetry of the WP_2 crystal structure, together with the consistence between the energies of the peaks observed in the polarized Raman spectra and the calculated Raman-active phonon energies, provides convincing evidence for the spatial inversion symmetry breaking in the type-II WSM candidate WP_2 . Our work not only opens a new avenue for the experimental identification of the type-II WSM state in WP_2 but also paves the way for developing a new generation of electronic devices based on the type-II WSMs with strong and tunable electrical anisotropy.

Experimental Section

Growth and Characterization of the WP_2 Single Crystals: The single crystals of WP_2 investigated in this paper were prepared via chemical vapor transport method.^[47] The WO_3 (Sigma-Aldrich, 99.995%), red phosphorus (Alfa Aesar, 99.999%), and iodine (Alfa Aesar, 99.99%) were sealed in an evacuated quartz tube. The quartz tube was placed in a tube furnace and gradually heated up to a temperature gradient of 970–850 °C. The reaction was held under this temperature gradient for 12 days. Then, the needle like WP_2 single crystals were obtained. The crystal structure of the as-grown single crystals was analyzed by single crystal X-ray diffractometer (BRUKER D8 VENTURE) with $MoK\alpha$ radiation (0.7 Å). The determined lattice parameters were $a = 3.17$ Å, $b = 11.18$ Å, and $c = 4.98$ Å, which were the same as the previous experimental studies.^[72,73] Figure S1 (Supporting Information) shows the indices of crystallographic plane of the WP_2 single crystals.

Angle-Resolved Polarized Raman Measurements: The angle-resolved polarized Raman measurements were performed in a backscattering geometry using a HORIBA LabRAM HR Evolution Raman spectrometer. The rotation angle of each step for the crystal-angle-resolved Raman experiments was 10°.

First-Principle Calculations: The first-principle calculations were performed using the Vienna ab initio simulation package^[74] with the generalized gradient approximation of the Perdew–Burke–Ernzerhof functional.^[75,76] The plane-wave kinetic energy cutoff of 520 eV and the $9 \times 9 \times 9$ Γ -centered k -point mesh were set. The atomic coordinates and the lattice shapes were fully relaxed until the Hellmann–Feynman forces on the atoms all were less than 0.01 eV Å^{−1} and the convergence criteria for energy was set at 10^{−8} eV. The initial lattice parameters of $a = 3.181$ Å, $b = 11.237$ Å, and $c = 5.007$ Å were used.^[77] To determine the phonon vibrational modes and phonon frequencies of WP_2 at the Brillouin zone center, the finite displacement method implemented in phonopy package was used.^[78] The electronic band structure of WP_2 shown in Figure 4c of the main text was calculated with considering spin–orbit coupling.

Electrical Resistivity Measurements: The electrical resistivity measurements were carried out in the low temperature superconducting magnet thermostat system (TKMS). The electrical resistivities were measured using a standard four-probe method with the electric currents applied along the a -axis and c -axis, respectively.

Optical Reflectance Measurements: The optical reflectance measurements were carried out on a Bruker Vertex 80v spectrometer in the energy range up to 25 000 cm^{−1}. The single-crystal samples were mounted on the optically black cone locating at the cold finger of a helium flow cryostat. An in situ gold and aluminum overcoating technique was employed to get the optical reflectance spectra $R(\omega)$. Linear polarizers were used for obtaining the linearly polarized incident light with its electric field of the incident light $E \parallel c$ -axis and $E \parallel a$ -axis. The optical reflectance data were highly reproducible.

Kramers–Kronig Transformation: A Kramers–Kronig transformation of the $R(\omega)$ of the WP_2 single crystals was used for getting the phase shift (i.e., $\theta(\omega)$) of the reflected light relative to the incident light according to the following relationship

$$\theta(\omega) = -\frac{\omega}{\pi} P \int_0^{+\infty} \frac{\ln R(\omega')}{\omega'^2 - \omega^2} d\omega' \quad (7)$$

where P denotes the Cauchy principal value. A Hagen–Rubens relation was used for low-energy extrapolation, and a $\omega^{-0.3}$ dependence was used for the high-energy extrapolation up to $300\,000\text{ cm}^{-1}$, above which a ω^{-4} dependence was employed. The $R(\omega)$ and $\theta(\omega)$ had the relationships with the real part $n(\omega)$ and the imaginary part $k(\omega)$ of the refractive index

$$n(\omega) = \frac{1 - R(\omega)}{1 + R(\omega) - 2\sqrt{R(\omega)}\cos(\theta(\omega))} \quad (8)$$

$$k(\omega) = \frac{-2\sqrt{R(\omega)}\sin(\theta(\omega))}{1 + R(\omega) - 2\sqrt{R(\omega)}\cos(\theta(\omega))} \quad (9)$$

Moreover, the real part $\sigma_1(\omega)$ and the imaginary part $\sigma_2(\omega)$ of the optical conductivity had the following relationships with $n(\omega)$ and $k(\omega)$

$$\sigma_1(\omega) = \frac{\omega n(\omega)k(\omega)}{2\pi} \quad (10)$$

$$\sigma_2(\omega) = \frac{\omega(1 - n^2(\omega) + k^2(\omega))}{4\pi} \quad (11)$$

Therefore, the real part $\sigma_1(\omega)$ and the imaginary part $\sigma_2(\omega)$ of the optical conductivity could be obtained when the $R(\omega)$ and $\theta(\omega)$ were gotten.

Extended Drude Analysis of the Optical Data: The scattering rate spectra $\tau^{-1}(\omega)$ could be obtained by performing the extended Drude analysis of the optical data according to Equation (12) in ref. [61]

$$\tau^{-1}(\omega) = \frac{\omega_p^2}{4\pi} \text{Re} \left(\frac{1}{\sigma(\omega)} \right) = \frac{\omega_p^2}{4\pi} \frac{\sigma_1(\omega)}{\sigma_1^2(\omega) + \sigma_2^2(\omega)} \quad (12)$$

where ω_p is the plasma frequency, $\sigma(\omega)$ is the complex optical conductivity, Re denotes the real part of the $1/\sigma(\omega)$, $\sigma_1(\omega)$ is the real part of the $\sigma(\omega)$, and $\sigma_2(\omega)$ is the imaginary part of the $\sigma(\omega)$. In the plasma frequency, the effective mass is an averaged mass of the charge carriers occupying the bands at Fermi energy.

Supporting Information

Supporting Information is available from the Wiley Online Library or from the author.

Acknowledgements

B.S., Y.S., and Y.H. contributed equally to this work. B.S. and Y.H. grew the single crystals. B.S., Y.H., and Y.Y. carried out the Raman measurements. B.S. did first-principle calculations and carried out the optical measurements. Y.S., X.C., B.S., and J.G. performed the transport experiments. B.S., J.Z., Y.M., J.L., and Z.-G.C. analyzed the data. B.S. and Z.-G.C. wrote the paper. Z.-G.C. conceived and supervised this project. The authors thank Rico U. Schoenemann, Fanming Qu, Di Chen, Meng Lv, Guang Yang, Nan Xu, and Quansheng Wu for their help and discussions. The authors acknowledge support from the National Key Research and Development Program of China (Grant Nos. 2017YFA0304700 and 2016YFA0300600) the Pioneer Hundred Talents Program of the Chinese Academy of Sciences and the National Science Foundation of China (Grant No. 51772322).

Conflict of Interest

The authors declare no conflict of interest.

Keywords

first-principle calculations, in-plane electrical anisotropy, optical spectroscopy, Raman spectroscopy, type-II Weyl semimetal

Received: June 2, 2019

Revised: September 2, 2019

Published online: September 18, 2019

- [1] X. Wan, A. M. Turner, A. Vishwanath, S. Y. Savrasov, *Phys. Rev. B* **2011**, *83*, 205101.
- [2] A. A. Burkov, L. Balents, *Phys. Rev. Lett.* **2011**, *107*, 127205.
- [3] H. Weng, C. Fang, Z. Fang, B. A. Bernevig, X. Dai, *Phys. Rev. X* **2015**, *5*, 011029.
- [4] S.-M. Huang, S.-Y. Xu, I. Belopolski, C.-C. Lee, G. Chang, B. Wang, N. Alidoust, G. Bian, M. Neupane, C. Zhang, S. Jia, A. Bansil, H. Lin, M. Z. Hasan, *Nat. Commun.* **2015**, *6*, 7373.
- [5] S.-Y. Xu, I. Belopolski, N. Alidoust, M. Neupane, G. Bian, C. Zhang, R. Sankar, G. Chang, Z. Yuan, C.-C. Lee, S.-M. Huang, H. Zheng, J. Ma, D. S. Sanchez, B. Wang, A. Bansil, F. Chou, P. P. Shibayev, H. Lin, S. Jia, M. Z. Hasan, *Science* **2015**, *349*, 613.
- [6] C. Shekhar, A. K. Nayak, Y. Sun, M. Schmidt, M. Nicklas, I. Leermakers, U. Zeitler, Y. Skourski, J. Wosnitzer, Z. Liu, Y. Chen, W. Schnelle, H. Borrmann, Y. Grin, C. Felser, B. Yan, *Nat. Phys.* **2015**, *11*, 645.
- [7] L. X. Yang, Z. K. Liu, Y. Sun, H. Peng, H. F. Yang, T. Zhang, B. Zhou, Y. Zhang, Y. F. Guo, M. Rahn, D. Prabhakaran, Z. Hussain, S.-K. Mo, C. Felser, B. Yan, Y. L. Chen, *Nat. Phys.* **2015**, *11*, 728.
- [8] Z. K. Liu, L. X. Yang, Y. Sun, T. Zhang, H. Peng, H. F. Yang, C. Chen, Y. Zhang, Y. F. Guo, D. Prabhakaran, M. Schmidt, Z. Hussain, S.-K. Mo, C. Felser, B. Yan, Y. L. Chen, *Nat. Mater.* **2016**, *15*, 27.
- [9] B. Q. Lv, N. Xu, H. M. Weng, J. Z. Ma, P. Richard, X. C. Huang, L. X. Zhao, G. F. Chen, C. E. Matt, F. Bisti, V. N. Strocov, J. Mesot, Z. Fang, X. Dai, T. Qian, M. Shi, H. Ding, *Nat. Phys.* **2015**, *11*, 724.
- [10] S.-Y. Xu, N. Alidoust, I. Belopolski, Z. Yuan, G. Bian, T.-R. Chang, H. Zheng, V. N. Strocov, D. S. Sanchez, G. Chang, C. Zhang, D. Mou, Y. Wu, L. Huang, C.-C. Lee, S.-M. Huang, B. Wang, A. Bansil, H.-T. Jeng, T. Neupert, A. Kaminski, H. Lin, S. Jia, M. Z. Hasan, *Nat. Phys.* **2015**, *11*, 748.
- [11] A. A. Zyuzin, A. A. Burkov, *Phys. Rev. B* **2012**, *86*, 115133.
- [12] M. M. Vazifeh, M. Franz, *Phys. Rev. Lett.* **2013**, *111*, 027201.
- [13] C.-X. Liu, P. Ye, X.-L. Qi, *Phys. Rev. B* **2013**, *87*, 235306.
- [14] X. Huang, L. Zhao, Y. Long, P. Wang, D. Chen, Z. Yang, H. Liang, M. Xue, H. Weng, Z. Fang, X. Dai, G. Chen, *Phys. Rev. X* **2015**, *5*, 031023.
- [15] C.-L. Zhang, S.-Y. Xu, I. Belopolski, Z. Yuan, Z. Lin, B. Tong, G. Bian, N. Alidoust, C.-C. Lee, S.-M. Huang, T.-R. Chang, G. Chang, C.-H. Hsu, H.-T. Jeng, M. Neupane, D. S. Sanchez, H. Zheng, J. Wang, H. Lin, C. Zhang, H.-Z. Lu, S.-Q. Shen, T. Neupert, M. Z. Hasan, S. Jia, *Nat. Commun.* **2016**, *7*, 10735.
- [16] M. Hirschberger, S. Kushwaha, Z. Wang, Q. Gibson, S. Liang, C. A. Belvin, B. A. Bernevig, R. J. Cava, N. P. Ong, *Nat. Mater.* **2016**, *15*, 1161.
- [17] K. Kuroda, T. Tomita, M.-T. Suzuki, C. Bareille, A. A. Nugroho, P. Goswami, M. Ochi, M. Ikhlas, M. Nakayama, S. Akebi, R. Noguchi, R. Ishii, N. Inami, K. Ono, H. Kumigashira, A. Varykhalov, T. Muro, T. Koretsune, R. Arita, S. Shin, T. Kondo, S. Nakatsuji, *Nat. Mater.* **2017**, *16*, 1090.

- [18] C. R. Rajamathi, U. Gupta, N. Kumar, H. Yang, Y. Sun, V. Süß, C. Shekhar, M. Schmidt, H. Blumtritt, P. Werner, B. Yan, S. Parkin, C. Felser, C. N. R. Rao, *Adv. Mater.* **2017**, 29, 1606202.
- [19] A. Politano, G. Chiarello, Z. Li, V. Fabio, L. Wang, L. Guo, X. Chen, D. Boukhvalov, *Adv. Funct. Mater.* **2018**, 28, 1800511.
- [20] G. Xu, H. Weng, Z. Wang, X. Dai, Z. Fang, *Phys. Rev. Lett.* **2011**, 107, 186806.
- [21] J. Ruan, S.-K. Jian, D. Zhang, H. Yao, H. Zhang, S.-C. Zhang, D. Xing, *Phys. Rev. Lett.* **2016**, 116, 226801.
- [22] A. A. Zyuzin, S. Wu, A. A. Burkov, *Phys. Rev. B* **2012**, 85, 165110.
- [23] Z. Wang, M. G. Vergniory, S. Kushwaha, M. Hirschberger, E. V. Chulkov, A. Ernst, N. P. Ong, R. J. Cava, B. A. Bernevig, *Phys. Rev. Lett.* **2016**, 117, 236401.
- [24] H. Yang, Y. Sun, Y. Zhang, W.-J. Shi, S. S. P. Parkin, B. Yan, *New J. Phys.* **2017**, 19, 015008.
- [25] J. Y. Liu, J. Hu, Q. Zhang, D. Graf, H. B. Cao, S. M. A. Radmanesh, D. J. Adams, Y. L. Zhu, G. F. Cheng, X. Liu, W. A. Phelan, J. Wei, M. Jaime, F. Balakirev, D. A. Tennant, J. F. DiTusa, I. Chiorescu, L. Spinu, Z. Q. Mao, *Nat. Mater.* **2017**, 16, 905.
- [26] S. Huang, J. Kim, W. A. Shelton, E. W. Plummer, R. Jin, *Proc. Natl. Acad. Sci. USA* **2017**, 114, 6256.
- [27] C. Guo, C. Cao, M. Smidman, F. Wu, Y. Zhang, F. Steglich, F.-C. Zhang, H. Yuan, *npj Quantum Mater.* **2017**, 2, 39.
- [28] A. A. Soluyanov, D. Gresch, Z. Wang, Q. Wu, M. Troyer, X. Dai, B. A. Bernevig, *Nature* **2015**, 527, 495.
- [29] Y. Sun, S.-C. Wu, M. N. Ali, C. Felser, B. Yan, *Phys. Rev. B* **2015**, 92, 161107(R).
- [30] Z. Wang, D. Gresch, A. A. Soluyanov, W. Xie, S. Kushwaha, X. Dai, M. Troyer, R. J. Cava, B. A. Bernevig, *Phys. Rev. Lett.* **2016**, 117, 056805.
- [31] G. Chang, S.-Y. Xu, D. S. Sanchez, S.-M. Huang, C.-C. Lee, T.-R. Chang, G. Bian, H. Zheng, I. Belopolski, N. Alidoust, H.-T. Jeng, A. Bansil, H. Lin, M. Z. Hasan, *Sci. Adv.* **2016**, 2, e1600295.
- [32] G. Autès, D. Gresch, M. Troyer, A. A. Soluyanov, O. V. Yazyev, *Phys. Rev. Lett.* **2016**, 117, 066402.
- [33] S.-Y. Xu, N. Alidoust, G. Chang, H. Lu, B. Singh, I. Belopolski, D. S. Sanchez, X. Zhang, G. Bian, H. Zheng, M.-A. Hsuanu, Y. Bian, S.-M. Huang, C.-H. Hsu, T.-R. Chang, H.-T. Jeng, A. Bansil, T. Neupert, V. N. Strocov, H. Lin, S. Jia, M. Z. Hasan, *Sci. Adv.* **2017**, 3, e1603266.
- [34] Y.-Y. Lv, X. Li, B.-B. Zhang, W. Y. Deng, S.-H. Yao, Y. B. Chen, J. Zhou, S.-T. Zhang, M.-H. Lu, L. Zhang, M. Tian, L. Sheng, Y.-F. Chen, *Phys. Rev. Lett.* **2017**, 118, 096603.
- [35] Z.-M. Yu, Y. Yao, S. A. Yang, *Phys. Rev. Lett.* **2016**, 117, 077202.
- [36] M. Udagawa, E. J. Bergholtz, *Phys. Rev. Lett.* **2016**, 117, 086401.
- [37] S. Tchoumakov, M. Civelli, M. O. Goerbig, *Phys. Rev. Lett.* **2016**, 117, 086402.
- [38] N. Kumar, Y. Sun, N. Xu, K. Manna, M. Yao, V. Süß, I. Leermakers, O. Young, T. Förster, M. Schmidt, H. Borrmann, B. Yan, U. Zeitler, M. Shi, C. Felser, C. Shekhar, *Nat. Commun.* **2017**, 8, 1642.
- [39] A. Wang, D. Graf, Y. Liu, Q. Du, J. Zheng, H. Lei, C. Petrovic, *Phys. Rev. B* **2017**, 96, 121107(R).
- [40] R. Schönemann, N. Aryal, Q. Zhou, Y.-C. Chiu, K.-W. Chen, T. J. Martin, G. T. McCandless, J. Y. Chan, E. Manousakis, L. Balicas, *Phys. Rev. B* **2017**, 96, 121108(R).
- [41] J. Gooth, F. Menges, N. Kumar, V. Süß, C. Shekhar, Y. Sun, U. Drechsler, R. Zierold, C. Felser, B. Gotsmann, *Nat. Commun.* **2018**, 9, 4093.
- [42] A. Jaoui, B. Fauqué, C. W. Rischau, A. Subedi, C. Fu, J. Gooth, N. Kumar, V. Süß, D. L. Maslov, C. Felser, K. Behnia, *npj Quantum Mater.* **2018**, 3, 64.
- [43] J. Coulter, R. Sundararaman, P. Narang, *Phys. Rev. B* **2018**, 98, 115130.
- [44] E. Razzoli, B. Zwartsenberg, M. Michiardi, F. Boschini, R. P. Day, I. S. Elfimov, J. D. Denlinger, V. Süß, C. Felser, A. Damascelli, *Phys. Rev. B* **2018**, 97, 201103(R).
- [45] M.-Y. Yao, N. Xu, Q. S. Wu, G. Autès, N. Kumar, V. N. Strocov, N. C. Plumb, M. Radovic, O. V. Yazyev, C. Felser, J. Mesot, M. Shi, *Phys. Rev. Lett.* **2019**, 122, 176402.
- [46] R. Loudon, *Adv. Phys.* **1964**, 13, 423.
- [47] R. Rühl, W. Jeitschko, *Monatsh. Chem.* **1983**, 114, 817.
- [48] J. H. Du, Z. F. Lou, S. N. Zhang, Y. X. Zhou, B. J. Xu, Q. Chen, Y. Q. Tang, S. J. Chen, H. C. Chen, Q. Q. Zhu, H. D. Wang, J. H. Yang, Q. S. Wu, V. O. Yazyev, M. H. Fang, *Phys. Rev. B* **2018**, 97, 245101.
- [49] L. Zhou, S. Huang, Y. Tatsumi, L. Wu, H. Guo, Y.-Q. Bie, K. Ueno, T. Yang, Y. Zhu, J. Kong, R. Saito, M. Dresselhaus, *J. Am. Chem. Soc.* **2017**, 139, 8396.
- [50] Y. Liu, Q. Gu, Y. Peng, S. Qi, N. Zhang, Y. Zhang, X. Ma, R. Zhu, L. Tong, J. Feng, Z. Liu, J.-H. Chen, *Adv. Mater.* **2018**, 30, 1706402.
- [51] Q. Song, X. Pan, H. Wang, K. Zhang, Q. Tan, P. Li, Y. Wan, Y. Wang, X. Xu, M. Lin, X. Wan, F. Song, L. Dai, *Sci. Rep.* **2016**, 6, 29254.
- [52] M. Kim, S. Han, J. H. Kim, J.-U. Lee, Z. Lee, H. Cheong, *2D Mater.* **2016**, 3, 034004.
- [53] S. Tongay, H. Sahin, C. Ko, A. Luce, W. Fan, K. Liu, J. Zhou, Y.-S. Huang, C.-H. Ho, J. Yan, D. F. Ogletree, S. Aloni, J. Ji, S. Li, J. Li, F. M. Peeters, J. Wu, *Nat. Commun.* **2014**, 5, 3252.
- [54] R. He, J.-A. Yan, Z. Yin, Z. Ye, G. Ye, J. Cheng, J. Li, C. H. Lui, *Nano Lett.* **2016**, 16, 1404.
- [55] K. Zhang, C. Bao, Q. Gu, X. Ren, H. Zhang, K. Deng, Y. Wu, Y. Li, J. Feng, S. Zhou, *Nat. Commun.* **2016**, 7, 13552.
- [56] S. Y. Chen, T. Goldstein, D. Venkataraman, A. Ramasubramaniam, J. Yan, *Nano Lett.* **2016**, 16, 5852.
- [57] R. Beams, L. G. Cançado, S. Krylyuk, I. Kalish, B. Kalanyan, A. K. Singh, K. Choudhary, A. Bruma, P. M. Vora, F. Tavazza, A. V. Davydov, S. J. Stranick, *ACS Nano* **2016**, 10, 9626.
- [58] J. Wang, X. Luo, S. Li, I. Verzhbitskiy, W. Zhao, S. Wang, S. Y. Quek, G. Eda, *Adv. Funct. Mater.* **2017**, 27, 1604799.
- [59] H. P. Hughes, R. H. Friend, *J. Phys. C: Solid State Phys.* **1978**, 11, L103.
- [60] D. H. Keum, S. Cho, J. H. Kim, D.-H. Choe, H.-J. Sung, M. Kan, H. Kang, J.-Y. Hwang, S. W. Kim, H. Yang, K. J. Chang, Y. H. Lee, *Nat. Phys.* **2015**, 11, 482.
- [61] D. N. Basov, T. Timusk, *Rev. Mod. Phys.* **2005**, 77, 721.
- [62] D. N. Basov, R. D. Averitt, D. van der Marel, M. Dressel, K. Haule, *Rev. Mod. Phys.* **2011**, 83, 471.
- [63] M. Dressel, G. Grüner, *Electrodynamics of Solids: Optical Properties of Electrons in Matter*, Cambridge University Press, Cambridge **2002**.
- [64] S. Y. Kim, M.-C. Lee, G. Han, M. Kratochvilova, S. Yun, S. J. Moon, C. Sohn, J.-G. Park, C. Kim, T. W. Noh, *Adv. Mater.* **2018**, 30, 1704777.
- [65] Z. G. Chen, T. Dong, R. H. Ruan, B. F. Hu, B. Cheng, W. Z. Hu, P. Zheng, Z. Fang, X. Dai, N. L. Wang, *Phys. Rev. Lett.* **2010**, 105, 097003.
- [66] Y. M. Dai, B. Xu, B. Shen, H. Xiao, H. H. Wen, X. G. Qiu, C. C. Homes, R. P. S. M. Lobo, *Phys. Rev. Lett.* **2013**, 111, 117001.
- [67] B. Xu, L. X. Zhao, P. Marsik, E. Sheveleva, F. Lyzwa, Y. M. Dai, G. F. Chen, X. G. Qiu, C. Bernhard, *Phys. Rev. Lett.* **2018**, 121, 187401.
- [68] Ya. I. Rodionov, K. I. Kugel, F. Nori, *Phys. Rev. B* **2015**, 92, 195117.
- [69] Q. Ma, S.-Y. Xu, C. K. Chan, C. L. Zhang, G. Q. Chang, Y. X. Lin, W. W. Xie, T. Palacios, H. Lin, S. Jia, A. L. Patrick, J. H. Pablo, G. Nuh, *Nat. Phys.* **2017**, 13, 842.
- [70] D. Sun, Z. K. Wu, D. Charles, X. B. Li, B. Claire, A. D. H. Walt, N. F. Phillip, B. N. Theodore, *Phys. Rev. Lett.* **2008**, 101, 157402.
- [71] J. W. Lai, Y. N. Liu, J. C. Ma, X. Zhuo, Y. Peng, W. Lu, Z. Liu, J. H. Chen, D. Sun, *ACS Nano* **2018**, 12, 4055.

- [72] H. Mathis, R. Glaum, R. Gruehn, *Acta Chem. Scand.* **1991**, 45, 781.
- [73] S. Rundqvist, T. Lundstrom, *Acta Chem. Scand.* **1963**, 17, 37.
- [74] G. Kresse, J. Furthmüller, *Phys. Rev. B* **1996**, 54, 11169.
- [75] J. P. Perdew, J. A. Chevary, S. H. Vosko, K. A. Jackson, M. R. Pederson, D. J. Singh, C. Fiolhais, *Phys. Rev. B* **1992**, 46, 6671.
- [76] J. P. Perdew, K. Burke, M. Ernzerhof, *Phys. Rev. Lett.* **1996**, 77, 3865.
- [77] A. Jain, S. P. Ong, G. Hautier, W. Chen, W. D. Richards, S. Dacek, S. Cholia, D. Gunter, D. Skinner, G. Cederand, K. A. Persson, *APL Mater.* **2013**, 1, 011002.
- [78] X. Gonze, C. Lee, *Phys. Rev. B* **1997**, 55, 10355.